

Towards understanding polar heat transport enhancement in sub-glacial oceans on icy moons

Robert Hartmann¹, Richard J. A. M. Stevens¹, Detlef Lohse^{1,2}, and Roberto Verzicco^{1,3,4}

¹Physics of Fluids Group and Twente Max Planck Center, J.M. Burgers Center for Fluid Dynamics,

University of Twente, 7500 AE Enschede, The Netherlands

²Max Planck Institute for Dynamics and Self-Organisation, 37077 Göttingen, Germany

³Dipartimento di Ingegneria Industriale, University of Rome 'Tor Vergata', 00133 Rome, Italy

⁴Gran Sasso Science Institute, 67100 L'Aquila, Italy

Key Points:

- The polar heat transport in spherical rotating Rayleigh-Bénard convection experiences an enhancement by rotation.
- The influence of rotation differs at low latitudes: the heat flux is reduced and compensates the polar enhancement on the global average.
- Enhanced polar heat transport due to Ekman pumping through axial vortices could explain various phenomena on icy moons.

17 **Abstract**

18 The interior oceans of several icy moons are considered as “moderately rotating”. Observations suggest a larger heat transport around the poles than at the equator. Rotating Rayleigh-Bénard convection (RRBC) in planar configuration is known to show an enhanced heat transport compared to the non-rotating case for such “moderate” rotation. We investigate the potential for such a (polar) heat transport enhancement in these sub-glacial oceans by direct numerical simulations of RRBC in spherical geometry for $Ra = 10^6$ and $0.7 \leq Pr \leq 4.38$. We find an enhancement up to 28% in the “polar tangent cylinder”, which is globally compensated by a reduced heat transport at low latitudes. As a result, the polar heat transport can exceed the equatorial by up to 50%. The enhancement is mostly insensitive to different radial gravity profiles, but decreases for thinner shells. In general, polar heat transport and its enhancement in spherical RRBC follow the same principles as in planar RRBC.

30 **Plain Language Summary**

31 The icy moons of Jupiter and Saturn like e.g., Europa, Titan, or Enceladus are believed
 32 to have a water ocean beneath their ice crust. Several of them show phenomena in their polar
 33 regions like active geysers or a thinner crust than at the equator, all of which might be related
 34 to a larger heat transport around the poles from the underlying ocean. We simulate the
 35 flow dynamics and currents in these sub-glacial ocean by high-fidelity simulations, though
 36 still at less extreme parameters than in reality, to study the heat transport and provide
 37 a possible explanation of such a ”polar heat transport enhancement”. We find that the
 38 heat transport around the poles can be up to 50% larger than around the equator, and
 39 that the believed properties of the icy moons and their oceans would allow polar heat
 40 transport enhancement. Therefore, our results may help to improve the understanding of
 41 ocean currents and latitudinal variations in the oceanic heat transport and crustal thickness
 42 on icy moons.

43 **1 Introduction**

44 In the common understanding, most icy satellites in the solar system, e.g., the Jovian
 45 and Saturnian moons Europa, Ganymede, Titan, and Enceladus, contain a global ocean layer
 46 beneath their ice crust (e.g., [Nimmo & Pappalardo, 2016](#)), which gained a lot of interest in
 47 terms of habitable environments (e.g., [Chyba & Hand, 2005](#); [Vance et al., 2018](#)). In order to
 48 asses their habitability, it is crucial to understand their flow dynamics. On Enceladus, for
 49 instance, eruptions from fault systems at the south pole (see, e.g., [Nimmo & Pappalardo,](#)
 50 [2016](#)) suggest a strong polar anomaly of enhanced heat transport. Furthermore, the crustal
 51 thickness counterintuitively decreases from the equator towards the poles (e.g., [Beuthe et](#)
 52 [al., 2016](#); [Čadek et al., 2019](#); [Hemingway & Mittal, 2019](#); [Kang, 2022](#); [Kang & Jansen,](#)
 53 [2022](#)), which suggests a large-scale latitudinal variation of the heat released from the sub-
 54 glacial ocean ([Kihoulou et al., 2023](#)). In this study, we investigate the dynamics inside and
 55 the heat transport out of these oceans by direct numerical simulations (DNSs) of rotating
 56 Rayleigh-Bénard convection (RRBC) in spherical geometry. Therewith, we aim to provide
 57 a possible explanation for the origin of the polar enhancement of the heat transport on icy
 58 moons.

59 The canonical system of RRBC in planar configuration has been extensively studied
 60 experimentally and numerically (see, e.g., the reviews by [Kunnen, 2021](#); [Ecke & Shishkina,](#)
 61 [2023](#); [Stevens et al., 2013](#); [Plumley & Julien, 2019](#), and Refs. therein). Its dynamical
 62 behavior is fully controlled by three dimensionless parameters: the Prandtl number Pr
 63 describing the fluid properties, the Rayleigh number Ra setting the strength of thermal
 64 driving, and the inverse Rossby number Ro^{-1} as a measure for the importance of rotation
 65 relative to buoyancy (full definitions in Sec. 2). The influence of rotation can alternatively
 66 be parameterized by the Ekman number $Ek = Ro\sqrt{Pr/Ra}$. Several flow regimes and

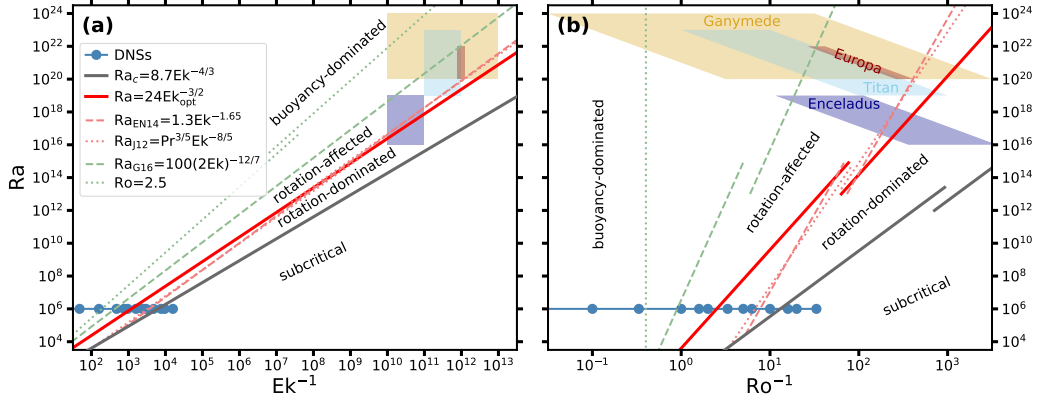


Figure 1. Regime diagram of (planar) RRBC in the parameter space of (a) Ra and Ek^{-1} and (b) Ra and Ro^{-1} (after Soderlund (2019), see also Kunnen (2021)): The solid gray line denotes the critical Rayleigh number Ra_c for the onset of convection (Chandrasekhar, 1961). The solid red line depicts the transition between the rotation-dominated and the rotation-affected regimes for based on boundary layer crossing and heat transport maximum per fixed Ra for $Pr > 1$ fluids (Yang et al., 2020). Dashed and dotted light red lines are alternative estimates for this transition by Ecke and Niemela (2014) and Julien, Knobloch, et al. (2012), respectively. The dashed and dotted green lines represent the transition between the rotation-affected and the buoyancy-dominated regimes based on Gastein et al. (2016) and for a cylinder with diameter-to-height ratio 1 (Weiss et al., 2010), respectively. The blue circles mark the simulations of spherical RRBC in this study ($Pr = 4.38$). The shaded areas show the predicted parameter range for several icy moons ($10 \leq Pr \leq 13$) as given in (Soderlund, 2019). Line offsets symbolize the Pr dependence of any transition between $Pr = 4.38$ like in our simulations and $Pr = 13$ like the upper bound for the icy moons.

flow states were discovered and studied over the past decades. The three major regimes based on the trend of heat transport with varying rotation are (i) the *buoyancy-dominated* regime at relatively slow rotation, where heat transport and flow dynamics remain unaffected compared to the non-rotating case, (ii) the transitional *rotation-affected* regime, where intermediate or moderate rotation starts to alter the flow, and (iii) the *rotation-dominated* regime for rapid rotation, where the heat transport steeply decreases with increasing rotation that impedes vertical motion (Proudman, 1916; Taylor, 1917), see e.g., Kunnen (2021) and Ecke and Shishkina (2023). Both rotation-affected and rotation-dominated regimes show a broad variety of sub-regimes or flow states, all of which are characterized by columnar vortical structures aligned with the rotation axis (e.g., Julien et al., 1996; Sprague et al., 2006; Stevens et al., 2009; Julien, Rubio, et al., 2012; Stellmach et al., 2014; Cheng et al., 2015; Aguirre Guzmán et al., 2020). Due to the huge variety of flow states, there exist various estimates for the boundaries of the above regimes in the literature (see Kunnen (2021) for a detailed overview) - most of them based on RRBC data in the classical planar configuration. The most common ones are summarized Fig. 1.

An important peculiarity of planar RRBC with $Pr > 1$ is that Ekman pumping through vertically coherent vortices enhances the heat transport in the rotation-affected regime to exceed its non-rotating value (e.g., Rossby, 1969; Kunnen et al., 2006; Zhong et al., 2009; Stevens et al., 2013). For not too large Ra , the enhancing effect is most efficient when thermal and kinetic boundary layers have approximately the same thickness (Stevens et al., 2010; Yang et al., 2020). This creates a heat transport maximum (per fixed Ra) that follows $Ra \propto Ek^{-3/2}$ (Fig. 1, red line; King et al., 2012; Yang et al., 2020). For very turbulent flows, the maximum diverges towards weaker rotation (Yang et al., 2020).

90 Based on the estimated parameter ranges for Europa, Ganymede, Titan, and Enceladus
 91 by Soderlund (2019), their sub-glacial oceans most likely are in the rotation-affected regime
 92 (see Fig. 1). Given that the water of these oceans has $Pr \in [10, 13]$ (Soderlund, 2019),
 93 they arguably have the potential for heat transport enhancement - at least around the
 94 poles, where buoyancy is mostly aligned with the rotation axis as it is in planar RRBC.
 95 Evidence of such a polar heat transport enhancement spherical RRBC are present in several
 96 studies (Soderlund, 2019; Amit et al., 2020; Bire et al., 2022). We therefore distinguish
 97 between two types of heat transport enhancement: (i) enhancement above the non-rotating
 98 heat transport in a specific region is considered as *polar/global/... enhancement*, whereas
 99 (ii) a larger heat transport at the poles than at the equator is referred to as *latitudinal
 100 enhancement*. Since most simulations of spherical RRBC are conducted for $Pr = 1$ (e.g.,
 101 Soderlund et al., 2012; Gastine et al., 2016; Wang et al., 2021) and all studies on rotation-
 102 induced heat transport enhancement focus on planar RRBC (e.g., Stevens et al., 2009, 2010;
 103 Weiss et al., 2016; Yang et al., 2020), we aim to bridge this gap and elucidate the potential
 104 of spherical RRBC to show polar and/or global heat transport enhancement. Therefore, we
 105 set $Pr = 4.38$ as in many simulations and experiments of planar RRBC and cover the entire
 106 range of regimes (Fig. 1).

107 In the following, we introduce spherical RRBC, its control parameters, and our
 108 numerical method (Sec. 2). Then, latitudinal variations of the heat transport are analyzed
 109 and linked to the predominant structures in the flow (Sec. 3). Subsequently, we discuss the
 110 importance of $Pr > 1$ by a direct comparison with $Pr \leq 1$ (Sec. 4), the influence of the shell
 111 thickness, i.e., the ocean depth (Sec. 5), the sensitivity to different radial gravity profiles
 112 (Sec. 6), and the relevance of the ratio between thermal and kinetic boundary layers for
 113 heat transport enhancement in spherical RRBC (Sec. 7). The letter ends with conclusions
 114 (Sec. 8).

115 2 Dynamical equations and numerical method

116 Spherical RRBC describes the dynamics of a fluid in a spherical shell confined by a hot
 117 inner and a cold outer sphere, rotating around a polar axis (Fig. 2(b)) (e.g., Roberts, 1968;
 118 Busse, 1970, 1983; Aurnou et al., 2015). The geometry of the system is determined by the
 119 inner and outer radii r_i and r_o , defining the shell thickness $H = r_o - r_i$ expressed by the
 120 radius ratio $\eta = r_i/r_o$. The dynamics are controlled by the three dimensionless parameters
 121 Pr , Ra , and Ro^{-1} , defined as:

$$122 \quad Pr = \frac{\nu}{\kappa} , \quad Ra = \frac{\alpha g_0 \Delta T H^3}{\nu \kappa} , \quad Ro^{-1} = \frac{2\Omega H}{\sqrt{\alpha g_0 \Delta T H}} . \quad (1)$$

123 Therein, ν is the kinematic viscosity, κ the thermal diffusivity, α the isobaric thermal
 124 expansion coefficient, g_0 the reference gravitational acceleration at the outer sphere, ΔT
 125 the temperature difference between inner and outer sphere, and Ω the angular rotation rate,
 126 respectively. Under Oberbeck-Boussinesq approximation, the system is governed by the
 127 continuity, Navier-Stokes and temperature convection-diffusion equations, which are given
 in dimensionless form as:

$$\nabla \cdot \vec{u} = 0 , \quad (2)$$

$$\frac{d\vec{u}}{dt} = -\nabla P + \sqrt{\frac{Pr}{Ra}} \nabla^2 \vec{u} + \Theta \frac{g(r)}{g_0} \vec{e}_r - \frac{1}{Ro} \vec{e}_z \times \vec{u} , \quad (3)$$

$$\frac{d\Theta}{dt} = \frac{1}{\sqrt{Pr Ra}} \nabla^2 \Theta . \quad (4)$$

128 Therein, \vec{u} , P , and Θ denote the normalized velocity, pressure, and temperature fields,
 129 respectively. d/dt denotes the full, so-called material derivative. $g(r) = g_0 (r/r_o)^\gamma$ accounts
 130 for radial variations in the gravity profile. The equations are normalized by H and the free-
 131 fall velocity $U_0 = \sqrt{\alpha g_0 \Delta T H}$. The temperature is normalized as $\Theta = \frac{T - T_{top}}{\Delta T} \in [0, 1]$. The
 132 pressure field P is reduced by the hydrostatic balance and centrifugal contributions. We

133 consider Coriolis forcing from constant rotation around the polar axis, but neglect centrifugal
 134 contributions on buoyancy. Isothermal and no-slip boundary conditions are imposed at the
 135 hot inner ($\Theta = 1$) and the cold outer ($\Theta = 0$) spheres.

136 In this study we conduct direct numerical simulations (DNSs) for $Ra = 10^6$ at $Pr =$
 137 4.38, 1 and 0.7 while varying the radius ratio η and gravity profile $g(r)$. The DNSs solve the
 138 governing equations (Eqs. 2-4) by a central second-order accurate finite-difference scheme
 139 based on a staggered grid discretization in spherical coordinates (Santelli et al., 2020),
 140 which has been rigorously validated in subsequent studies (Wang et al., 2021, 2022). The
 141 computational grid is uniformly spaced in the longitudinal and latitudinal directions, while
 142 the grid points in the radial direction are clustered towards the inner and outer spheres.
 143 This ensures an appropriate resolution of the Kolmogorov scales in the bulk, as well as of the
 144 boundary layers (Shishkina et al., 2010). A summary of grid sizes and numerical parameters
 145 can be found in the Supporting Information (Text S1, Tabs. S1-S3).

146 3 Polar heat transport enhancement

147 We begin our investigation on a rather thick shell of $\eta = 0.6$ with a constant gravity
 148 $g(r) = g_0$. The dimensionless heat transport is given by the Nusselt number Nu . We first
 149 consider Nu on the outer sphere as a function of the latitude φ :

$$150 \quad Nu_{r_o}(|\varphi|) = -\frac{1}{\eta} \partial_r \langle \Theta \rangle_{t,\vartheta,\pm\varphi} \Big|_{r_o}. \quad (5)$$

150 Therein $\langle \cdot \rangle_{t,\vartheta,\pm\varphi}$ indicates averaging in time, longitude, and latitudinal symmetry around
 151 the equator. For no and slow rotation ($Ro^{-1} \leq 0.3$), the heat transport is expectably
 152 uniform over φ (Fig. 2(a)). Accordingly, the flow is dominated by radial buoyant plumes
 153 (Fig. 2(c)), which can organize in a persistent large-scale circulation pattern. Such large-
 154 scale circulations are well known from other non-rotating geometries, e.g., RBC in cylindrical
 155 containers (e.g., Ahlers et al., 2009, and Refs. therein), 2D RBC (e.g., van der Poel et al.,
 156 2013, and Refs. therein), or extremely wide domains (Stevens et al., 2018). However,
 157 without rotation, the heat transport ideally is radially symmetric, defining a reference value
 158 $Nu_0 = \langle Nu_{r_o} \rangle_\varphi (Ro^{-1} = 0)$ (Fig. 2(a), horizontal dashed line).

159 At intermediate rotation rates ($1 \leq Ro^{-1} \leq 5$), the heat transport is reduced to-
 160 wards the equator and enhanced towards the poles compared to the non-rotating reference
 161 (Fig. 2(a)). Taylor columns aligned with the rotation axis form in the flow (Fig. 2(d)) and
 162 alter the heat transport. Their vortical motion impedes the radial heat transport around
 163 the equator and leads to the formation of sheet-like thermal plumes around the columnar
 164 structures (similar to Soderlund et al., 2012; Aurnou et al., 2015). On the contrary, the
 165 Taylor columns support the radial heat transport around the poles by Ekman pumping
 166 through their interior (in presence of no-slip boundary conditions, e.g., Stellmach et al.
 167 (2014)). For $\eta = 0.6$, the polar tangent cylinder, i.e., the cylinder around the inner sphere
 168 aligned with the polar axis, intersects with the outer sphere at latitude $|\varphi_{tc}| = 53.13^\circ$. We
 169 use $|\varphi_{tc}|$ to distinguish between the “polar region” ($|\varphi_{tc}| < |\varphi| < 90^\circ$), in which ideal axial
 170 Taylor columns connect the hot inner sphere with cold outer sphere, and the “low latitude
 171 region” ($|\varphi_{tc}| > |\varphi| > 0^\circ$), in which axial Taylor columns connect the Northern and Southern
 172 hemispheres of the outer sphere (Fig. 2(b)). For $1 \leq Ro^{-1} \leq 5$, $|\varphi_{tc}|$ clearly correlates
 173 with the transition from reduced to enhanced heat transport ($Nu_{r_o}(|\varphi_{tc}|) \approx Nu_0$). The
 174 rather smooth trend of $Nu_{r_o}(|\varphi|)$ across $|\varphi_{tc}|$ however suggests that the inclination between
 175 buoyancy (radial) and rotation (axial) additionally influences the enhancement with latitude.

176 For rapid rotation ($Ro^{-1} \geq 10$), the latitudinal trend in the heat transport is inverted
 177 (Fig. 2(a)). At high latitudes, the heat transport quickly decreases with increasing Ro^{-1}
 178 down to $Nu_{r_o} = 1$. Towards the equator, the heat transport first increases slightly (com-
 179 pared to the reduction at intermediate rotation), before it also decreases with increasing
 180 Ro^{-1} . With increasing rotation the fluid motion is suppressed in the axial direction and

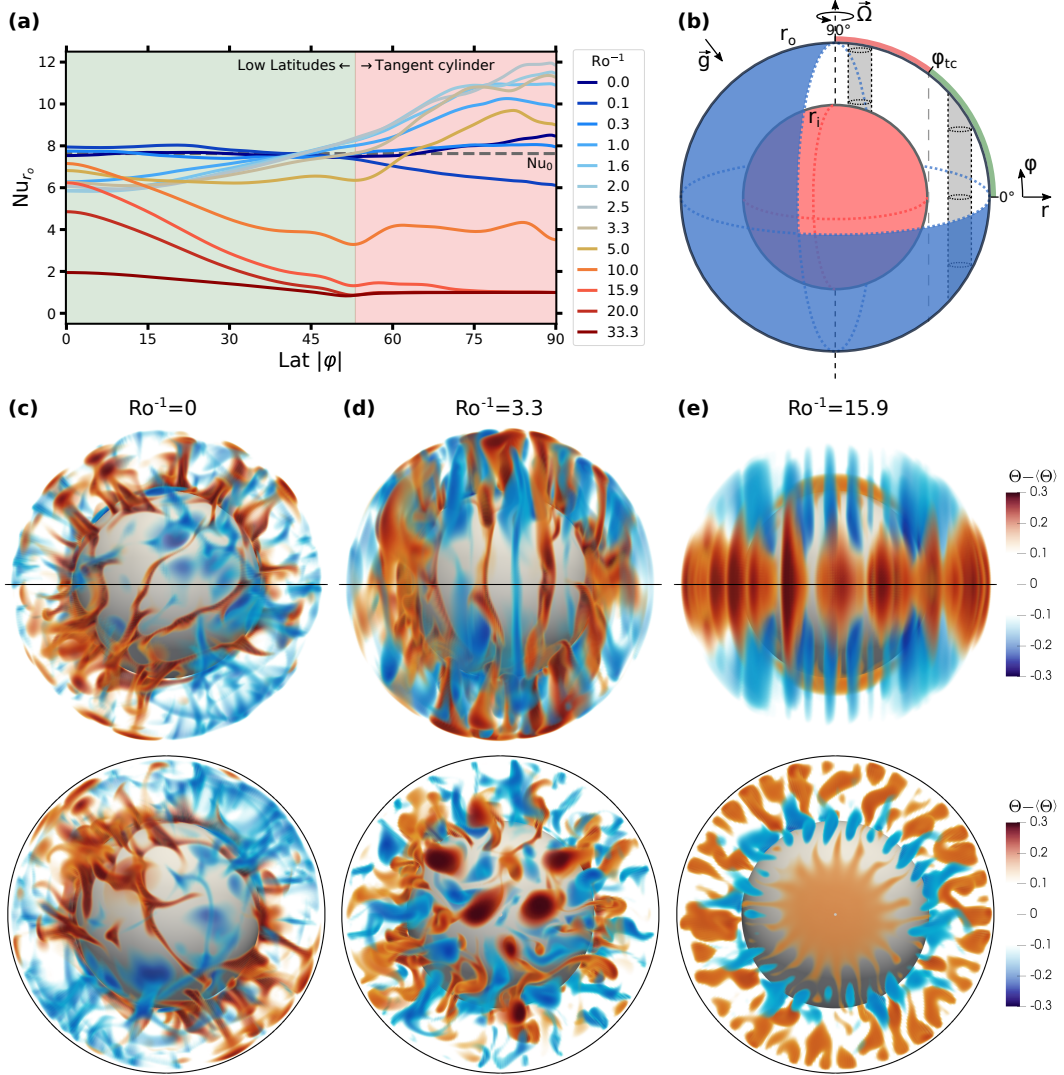


Figure 2. (a) Dimensionless heat transport at the outer sphere Nu_{r_o} as function of the latitude $|\varphi|$ for various rotation rates Ro^{-1} at $Ra = 10^6$ and $Pr = 4.38$ with $\eta = 0.6$ and constant $g(r) = g_0$. (b) Schematic view on spherical RRBC showing the idealized arrangement of axially aligned Taylor columns inside and outside the polar tangent cylinder. (c-e) Corresponding 3D snapshots of the temperature fluctuations $\Theta' = \Theta - \langle \Theta \rangle_{\theta, \varphi}$ at no rotation ($Ro^{-1} = 0$), intermediate rotation ($Ro^{-1} = 3.3$), and rapid rotation ($Ro^{-1} = 15.9$), respectively, viewed from the equator (top) and the South pole (bottom).

181 becomes strongly focused in the orthogonal planes (Proudman, 1916; Taylor, 1917, 1923).
 182 Thus, convection halts inside the tangent cylinder and the radial heat transport mostly
 183 aligned with the rotation axis becomes purely conductive. Towards the equator, quasi-2D
 184 vortical motion aligns with radial buoyancy, which helps to longer sustain convective heat
 185 transport via sheet-like plumes (Fig. 2(e)). Also for rapid rotation, $|\varphi_{tc}|$ depicts a major
 186 transition in the trend of $Nu_{r_o}(|\varphi|)$, namely where the heat transport starts to increase
 187 towards its equatorial peak value (Fig. 2(a), see also Wang et al., 2021; Gastine & Aurnou,
 188 2023).

189 Overall, Fig. 2 shows that heat transport enhancement, as known from planar RRBC, is
 190 limited to high latitudes inside the tangent cylinder in spherical RRBC. In order to further
 191 quantify the polar enhancement, we consider the radial heat transport at the outer sphere
 192 averaged (i) over the polar region $Nu_{tc} = \langle Nu_{r_o} \rangle_{|\varphi| > |\varphi_{tc}|}$, (ii) in the complementary low
 193 latitude region $Nu_{ll} = \langle Nu_{r_o} \rangle_{|\varphi| < |\varphi_{tc}|}$, and (iii) globally over the entire sphere $\langle Nu_{r_o} \rangle_\varphi$.
 194 In this way, we can demonstrate that the heat transport in the polar region Nu_{tc} shows
 195 the typical enhancement behavior of planar RRBC (Fig. 3(a), red triangles). Together
 196 with the results above (Fig. 2), it becomes clear that the basic mechanisms, which cause
 197 the polar enhancement, remain the same, namely: the formation of axially coherent vortical
 198 structures bridging the bulk between the hot and the cold source, such that Ekman pumping
 199 of relatively hot/cold fluid from the boundary layers can support the heat transport along
 200 the axial direction. However, no enhancement is found for the global heat transport of the
 201 full Rayleigh-Bénard sphere (Fig. 3(a), gray circles). The enhanced heat transport inside
 202 the polar region is globally balanced by the reduced heat transport in the low latitude region
 203 (Fig. 3(a), green squares). It seems that the equatorial reduction strengthens as the polar
 204 enhancement increases.

205 The amplitude of polar heat transport enhancement compared to Nu_0 reaches \approx 28% (Fig. 3(a), red triangles), which is comparable with the enhancement observed in
 206 planar RRBC (e.g., Zhong et al., 2009; Kunnen et al., 2011; Yang et al., 2020). The
 207 polar enhancement is even larger when only a narrower region directly around the poles is
 208 considered (see Supporting Information Fig. S1), which emphasizes the additional influence
 209 of the tilt between buoyancy and rotation. Despite the absence of a global heat transport
 210 enhancement (relative to Nu_0 of the non-rotating system), the spatial large-scale variations
 211 of the heat transport are more important in geo- and astrophysical contexts, like the ocean
 212 dynamics of the icy moons. A direct comparison of Nu_{tc}/Nu_{ll} yields up to $\approx 50\%$ larger
 213 heat transport in the polar region than in the low latitude region at the maximal polar
 214 enhancement (Fig. 3(b), full circles). For strong rotation this ratio inverts as convection
 215 halts earlier in the tangent cylinder and will again saturate at 1 once the system is fully in
 216 rest (Gastine & Aurnou, 2023).

218 4 Dependence on the Prandtl number

219 Heat transport enhancement relative to Nu_0 in planar RRBC essentially depends on
 220 Pr . No clear enhancement due to rotation is observed for $Pr < 1$ as the thermal boundary
 221 layer is always thinner than the kinetic Ekman layer (Stevens et al., 2010; Yang et al., 2020).
 222 To validate this Pr dependence, we conducted additional series of DNSs for $Pr = 1$ and
 223 0.7 (see Supporting Information Tab. S3). As expected, the heat transport enhancement
 224 Nu/Nu_0 inside the polar tangent cylinder of spherical RRBC vanishes (see Supporting
 225 Information Fig. S2(a)). Interestingly, the heat transport in the low-latitude region also
 226 decreases with smaller Pr . Therefore, we can still observe some latitudinal enhancement
 227 $Nu_{tc}/Nu_{ll} > 1$ for $Pr = 0.7$ (see Supporting Information Fig. S2(b)) without any polar
 228 enhancement $Nu/Nu_0 < 1$. This agrees with the results from Soderlund (2019) performed
 229 at $Pr = 1$. However, the latitudinal enhancement Nu_{tc}/Nu_{ll} is significantly smaller than for
 230 $Pr = 4.38$. Based on this trend, we conclude that, the polar enhancement Nu/Nu_0 , which
 231 typically intensifies with increasing Pr above unity, will additionally amplify the latitudinal
 232 enhancement Nu_{tc}/Nu_{ll} . Since Pr also affects the heat transport in the low latitude region,

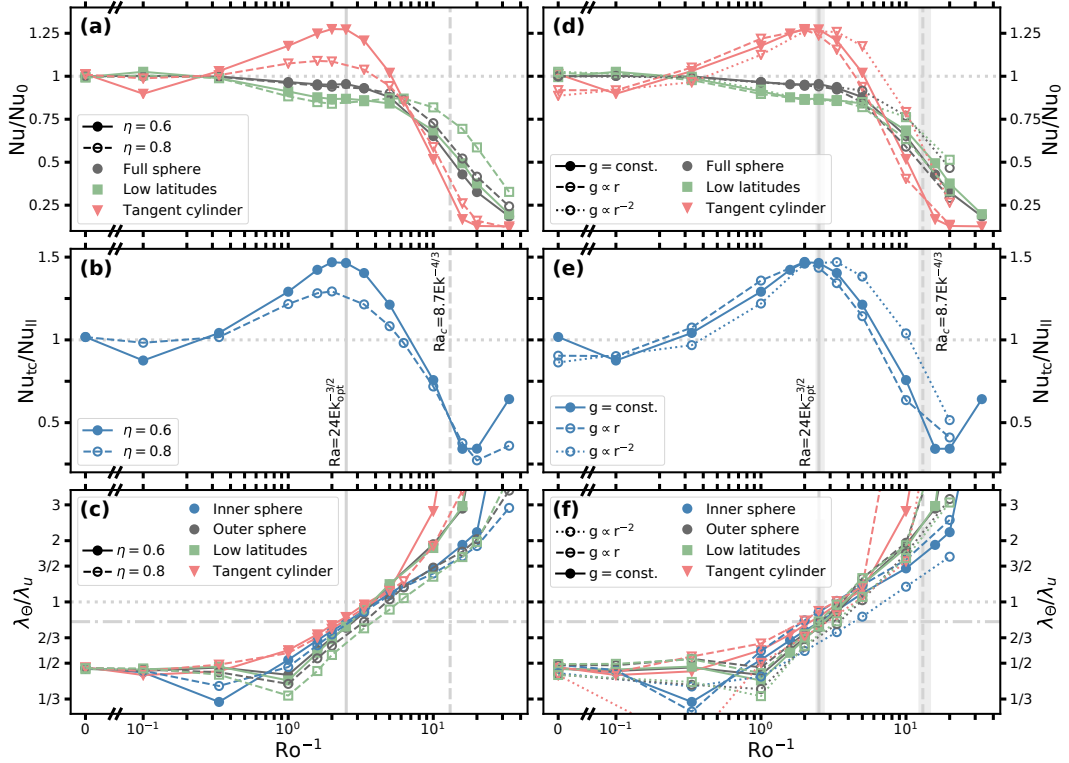


Figure 3. (a,d) Heat transport Nu relative to the non-rotating reference Nu_0 as a function of Ro^{-1} for the full sphere ($Nu \equiv \langle Nu_{r_o} \rangle_\varphi$), in the polar region ($Nu_{tc} = \langle Nu_{r_o} \rangle_{|\varphi| > |\varphi_{tc}|}$), and in the complementary low latitude region ($Nu_{ll} = \langle Nu_{r_o} \rangle_{|\varphi| < |\varphi_{tc}|}$). (b,e) Ratio between the heat transport in the polar region Nu_{tc} and the low latitude region Nu_{ll} as a function of Ro^{-1} . (c,f) Ratio of thermal and kinetic boundary layer thicknesses λ_Θ/λ_u as a function of Ro^{-1} averaged over the inner sphere, the outer sphere, the polar region, and the low latitude region. (left) For different η with constant $g(r) = g_0$, and (right) for different $g(r) \propto r^\gamma$ with fixed $\eta = 0.6$. All data at $Pr = 4.38$, $Ra = 10^6$. The solid and dashed vertical lines mark the predicted optimal rotation rate Ro_{opt}^{-1} in planar RRBC given by $Ra = 24E^{k^{-3/2}}$ (Yang et al., 2020; King et al., 2012) and the predicted onset of convection in planar RRBC given by $Ra_c = 8.7E^{k^{-4/3}}$ (Chandrasekhar, 1961), respectively. The influence of Ra_{eff} on these transitions (shaded areas) are very limited (see Sec. 6, 7). The dotted and dashed-dotted horizontal lines emphasize ratio 1 and 0.8, respectively.

233 we speculate that for $Pr \gg 1$, even an enhancement of the global heat transport Nu/Nu_0
 234 is possible.

235 5 Influence of shell thickness

236 In fact, the oceans of icy satellites are much thinner water layers, i.e., characterized by a
 237 much larger radius ratio than the previous $\eta = 0.6$. For the popular icy satellites indicated in
 238 Fig. 1, the estimates are in a range of $0.74 < \eta < 0.99$ (Vance et al., 2018; Soderlund, 2019).
 239 A larger η also results in a larger polar tangent cylinder, in which the axial columns connect
 240 inner and outer sphere. When we increase the radius ratio to $\eta = 0.8$, the tangent cylinder
 241 starts already at $\varphi_{tc} \approx 36.87$ (compared to $\varphi_{tc} \approx 53.13$ for $\eta = 0.6$). Interestingly, the heat
 242 transport enhancement in the polar tangent cylinder drops to only $\approx 9\%$, whereas the full
 243 sphere average remains unchanged throughout the rotation-affected regime (Fig. 3(a), open
 244 symbols). This seems very counterintuitive since one would rather expect that a constant
 245 enhancement amplitude in the enlarged tangent cylinder, which also affects the global heat
 246 transport. We speculate that increasing inclination between radial buoyancy and axial
 247 rotation towards the edge of the tangent cylinder reduces the efficiency of vortices pumping
 248 heat in the axial direction. However, we note that even at the poles the heat transport
 249 enhancement is smaller for $\eta = 0.8$ than for $\eta = 0.6$. (see Supporting Information Fig. S3).
 250 Regardless, the heat transport in the polar region can still be significantly larger than at
 251 the equator for $\eta = 0.8$, resulting in a latitudinal enhancement up to $\approx 25\%$ (Fig. 3(b),
 252 open symbols). The optimal rotation rate Ro_{opt}^{-1} at which the maximal enhancements are
 253 achieved, however, remains mostly unaffected.

254 In the rotation-dominated regime, the heat transport in the polar region decreases
 255 similarly with Ro^{-1} for both η . Convection in the tangent cylinder ceases around $Ro_c^{-1} =$
 256 $8.7^{-3/4} Pr^{1/2} Ra^{1/4} \approx 13.06$ (Fig. 3(a), vertical dashed line), derived from the predicted
 257 critical Rayleigh number $Ra_c = 8.7 Ek^{-4/3}$ in planar RRBC (Chandrasekhar, 1961). On
 258 the contrary, faster rotation is necessary to suppress convective heat transport in the low
 259 latitude region for larger η . Consequently, the equatorial onset of convection in spherical
 260 RRBC additionally depends on η , in contrast to Ra_c in planar RRBC valid in the likewise
 261 oriented tangent cylinder. Together with the data from Gastine et al. (2016) and Gastine
 262 and Aurnou (2023), this reflects that the equatorial onset of convection in spherical RRBC is
 263 different than in planar RRBC, i.e., $Ra_{c,sp} = f(\eta, \dots) Ek^{-4/3}$ rather than $Ra_c = 8.7 Ek^{-4/3}$.

264 Lastly, we note the different slopes of the heat transport in the polar and the low
 265 latitude region in the rotation-dominated regime. They can be attributed to “steep scaling”
 266 $Nu \propto (Ra Ek^{4/3})^3 \propto Ro^4$ in the polar region where Ekman pumping plays an active role
 267 (King et al., 2012, 2013; Julien et al., 2016; Plumley et al., 2016; Gastine & Aurnou, 2023)
 268 and (the onset of) “diffusion-free scaling” $Nu \propto (Ra Ek^{4/3})^{3/2} \propto Ro^2$ (Gastine et al.,
 269 2016; Wang et al., 2021). More detailed evidence for this can be found in the Supporting
 270 Information (Text S2, Fig. S4).

271 6 Sensitivity to different gravity profiles

272 We further investigate the influence of different radial gravity profiles $g(r) = g_0 (r/r_o)^\gamma$.
 273 Besides a constant gravity ($\gamma = 0$), we apply a homogeneous self-gravitating profile ($\gamma = 1$)
 274 and a mass-centered profile ($\gamma = -2$). For this, we stick to $\eta = 0.6$, because the radial gravity
 275 variation is larger in thicker shells and so is its expected impact on the heat transport. Aside
 276 from minor deviations, we cannot observe major differences in the normalized heat transport
 277 Nu/Nu_0 in the rotation-affected regime (until the polar heat transport maximum), including
 278 the amplitude of the polar and latitudinal enhancement maxima and their optimal rotation
 279 rate Ro_{opt}^{-1} (Fig. 3(d,e)). One might spot a small shift in Ro^{-1} with γ . Its trend likely
 280 arises from a change of the effective Rayleigh number of the system $Ra_{eff} = \langle Ra(r) \rangle_r$,
 281 when the gravity varies with r : $Ra_{eff}(\gamma = 1) < R_{eff}(\gamma = 0) = Ra < R_{eff}(\gamma = -2)$ (see
 282 Supporting Information Text S3). Solely in the rotation-dominant regime (beyond the polar

heat transport maximum), the heat transport remains considerably larger for smaller γ , i.e., increasing Ra_{eff} . Thus, the relative heat transport enhancement Nu/Nu_0 for $Ro^{-1} \leq Ro_{\text{opt}}^{-1}$ is mostly unaffected by the gravity profile $g(r) = r^\gamma$, in contrast to the absolute values Nu (Gastine et al., 2015; Wang et al., 2022). Especially the amplitude of the polar enhancement maximum Nu_{\max}/Nu_0 seems to be insensitive to $g(r)$.

288 7 Relevance of the boundary layer ratio

289 In planar RRBC, the heat transport maximum for not too large Ra is typically associated
 290 with an equal thickness of the thermal and kinetic boundary layers λ_Θ and λ_u (Stevens
 291 et al., 2010), which theoretically scales as $\lambda_\Theta/\lambda_u \propto Ek^{3/2}Ra$ (King et al., 2012) giving an
 292 estimate for the optimal rotation rate at relatively low Ra (Yang et al., 2020):
 293

$$Ro_{\text{opt}}^{-1} \approx 0.12 Pr^{1/2} Ra^{1/6} \quad \text{or} \quad Ra \approx 24 Ek_{\text{opt}}^{-3/2}. \quad (6)$$

293 The predicted Ro_{opt}^{-1} nicely aligns with the heat transport maxima in the polar tangent
 294 cylinder independent of η and $g(r)$ (Fig. 3(a,d), solid vertical line). Taking Ra_{eff} into
 295 account yields $Ro_{\text{opt},\gamma=1}^{-1} \approx 0.97 Ro_{\text{opt},\gamma=0}^{-1}$ and $Ro_{\text{opt},\gamma=-2}^{-1} \approx 1.07 Ro_{\text{opt},\gamma=0}^{-1}$ (see Supporting
 296 Information Text S3). Both predicted and observed shifts of Ro_{opt}^{-1} with γ are mostly
 297 negligible.

298 We further verify the predicted boundary layer crossing by directly computing λ_Θ and
 299 λ_u from our DNSs as the height of the first peak in the radial profiles of the laterally averaged
 300 root-mean-square temperature and lateral velocity, respectively. Due to the asymmetry of
 301 cooling and heating in spherical RRBC, the boundary layer thicknesses differ between inner
 302 and outer sphere (Gastine et al., 2015). Therefore, we consider λ_Θ and λ_u separately
 303 averaged over (i) the inner and (ii) the outer spheres. In addition to the spatial average
 304 over the full spheres, we again distinguish between (iii) the polar and (iv) the low latitude
 305 regions on the outer sphere. Our data confirms such a typical boundary layer crossing for all
 306 the regions (i)-(iv) in the spherical geometry – independent of η (Fig. 3(c)). Furthermore,
 307 the polar heat transport maxima and the predicted Ro_{opt}^{-1} perfectly match to an observed
 308 boundary layer ratio of $\lambda_\Theta/\lambda_u \approx 0.8$ (dotted horizontal line), especially for the polar region
 309 (red symbols) and the inner sphere (blue symbols). This fully agrees with the observations
 310 of Yang et al. (2020) in planar RRBC based on the same boundary layer definitions. Only
 311 for the thinner $\eta = 0.8$ shell, the boundary layer ratio of the low latitude region (and
 312 consequently also for the full outer sphere) lie slightly below the expected $\lambda_\Theta/\lambda_u \approx 0.8$.
 313 We also relate this to the different flow orientation at the equator, where the inner and
 314 outer shells act more like a sidewall for the axial vortex structures compared to the classical
 315 configuration in planar RRBC and the alike tangent cylinder. It therefore is even more
 316 remarkable that the boundary layer ratio also matches for the low latitude region in the
 317 other cases. For variations of $g(r)$, the agreement with 0.8 is still very good (Fig. 3(f)).
 318

8 Conclusions

319 Our DNSs of spherical RRBC with Pr larger than unity ($Pr = 4.38$) confirm the main
 320 features of heat transport enhancement, as known from planar RRBC, to similarly occur in
 321 the spherical geometry:

- 322 (i) The three major regimes (buoyancy-dominated, rotation-affected, rotation-dominated)
 323 for the heat transport behavior of RRBC can be identified (Kunnen, 2021; Ecke &
 324 Shishkina, 2023).
- 325 (ii) *Intermediate* rotation enhances the heat transport up to $\approx 28\%$ compared to the
 326 non-rotating case inside the polar tangent cylinder, where buoyancy is mostly aligned
 327 with the rotation axis and axially coherent vortices (Taylor columns) connect the hot
 328 inner with the cold outer shell.

- 330 (iii) The maximal (polar) enhancement is determined by an equal thickness of the thermal
 331 and kinetic boundary layers $\lambda_\Theta/\lambda_u \approx 1$. The associated optimal rotation rate
 332 $Ro_{\text{opt}}^{-1} \Leftrightarrow Ek_{\text{opt}}^{-1}$ can still be predicted via $Ra \approx 24 Ek^{-3/2}$ as in planar RRBC (King
 333 et al., 2012; Yang et al., 2020).
- 334

335 We however find that the polar heat transport enhancement is accompanied by a reduced
 336 heat transport at low latitudes outside the tangent cylinder, where buoyancy is mostly
 337 orthogonal to the rotation axis and the axially coherent vortices can only connect both
 338 hemispheres of the cold outer shell. The equatorial reduction compensates the polar
 339 enhancement on the global average on the one hand, which on the other hand results in an
 340 even larger latitudinal enhancement of up to $\approx 50\%$ between the polar and the low latitude
 341 region.

342 We further clarified that the relative heat transport enhancements Nu/Nu_0 and $Nu_{\text{tc}}/Nu_{\text{ll}}$
 343 are mostly unaffected by the radial gravity profile. Rather surprisingly, a thinner shell
 344 ($\eta = 0.8$), which comes along with a larger tangent cylinder, shows less but still significant
 345 enhancement ($\approx 9\%$ for Nu/Nu_0 and $\approx 25\%$ for $Nu_{\text{tc}}/Nu_{\text{ll}}$). The fact that the polar
 346 enhancement decreases to remain balanced by the equatorial reduction depicts a non-trivial
 347 coupling between the polar and the low latitude region in spherical RRBC.

348 The existence of polar heat transport enhancement in spherical RRBC, which increases
 349 the latitudinal difference between polar and equatorial heat transport, implies that ac-
 350 counting for $Pr > 1$ can be crucial for simulations of icy satellite oceans. Heat transport
 351 enhancement on the one hand increases with larger Pr (e.g., Zhong et al., 2009; Stevens et
 352 al., 2010) but on the other hand decreases with larger Ra (e.g., Yang et al., 2020). Hence, the
 353 question on how much enhancement persists on icy satellites with $Pr > 4.38$ ($10 \lesssim Pr \lesssim 13$)
 354 and $Ra \gg 10^6$ ($10^{16} \lesssim Ra \lesssim 10^{24}$) needs to be addressed differently as DNS cannot reach
 355 these parameters. However, our findings show, in line with evidences from previous studies
 356 (Soderlund, 2019; Amit et al., 2020; Bire et al., 2022), that in principle large Pr related
 357 heat transport enhancement could serve as an explanation for latitudinal heat transport and
 358 associated ice thickness variations on icy satellites.

359 Open Research Section

360 Data availability statement

361 The data that support the findings of this study are openly available in *4TU.ResearchData*
 362 at http://doi.org/tba_on_publication.

363 Acknowledgments

364 This work was funded by the ERC Starting Grant *UltimateRB* No. 804283. We acknowledge
 365 the access to several computational resources, all of which were used for this work: PRACE
 366 for awarding us access to MareNostrum4 at the Barcelona Supercomputing Center (BSC),
 367 Spain and IRENE at Très Grand Centre de Calcul (TGCC) du CEA, France (project
 368 2021250115), and EuroHPC for awarding us access to Discoverer at Sofiatech, Bulgaria
 369 (No. EHPC-REG-2022R03-208).

370 References

- 371 Aguirre Guzmán, A. J., Madonia, M., Cheng, J. S., Ostilla-Mónico, R., Clercx, H. J., &
 372 Kunnen, R. P. (2020). Competition between Ekman Plumes and Vortex Condensates
 373 in Rapidly Rotating Thermal Convection. *Phys. Rev. Lett.*, *125*, 214501.
- 374 Ahlers, G., Grossmann, S., & Lohse, D. (2009). Heat transfer and large scale dynamics in
 375 turbulent Rayleigh-Bénard convection. *Rev. Mod. Phys.*, *81*, 503–537.
- 376 Amit, H., Choblet, G., Tobie, G., Terra-Nova, F., Čadek, O., & Bouffard, M. (2020). Cooling

- 377 patterns in rotating thin spherical shells — Application to Titan’s subsurface ocean.
 378 *ICARUS*, 338, 113509.
- 379 Aurnou, J., Calkins, M., Cheng, J., Julien, K., King, E., Nieves, D., ... Stellmach, S.
 380 (2015). Rotating convective turbulence in Earth and planetary cores. *Phys. Earth
 381 Planet. Inter.*, 246, 52–71.
- 382 Beuthe, M., Rivoldini, A., & Trinh, A. (2016). Enceladus’s and Dione’s floating ice shells
 383 supported by minimum stress isostasy. *Geophys. Res. Lett.*, 43(19), 10,088–10,096.
- 384 Bire, S., Kang, W., Ramadhan, A., Campin, J., & Marshall, J. (2022). Exploring Ocean
 385 Circulation on Icy Moons Heated From Below. *J. Geophys. Res. Planets*, 127(3).
- 386 Busse, F. H. (1970). Thermal instabilities in rapidly rotating systems. *J. Fluid Mech.*,
 387 44(3), 441–460.
- 388 Busse, F. H. (1983). A model of mean zonal flows in the major planets. *Geophys. Astrophys.
 389 Fluid Dyn.*, 23(2), 153–174.
- 390 Chandrasekhar, S. (1961). *Hydrodynamic and hydromagnetic stability*. Oxford University
 391 Press.
- 392 Cheng, J. S., Stellmach, S., Ribeiro, A., Grannan, A., King, E. M., & Aurnou, J. M.
 393 (2015). Laboratory-numerical models of rapidly rotating convection in planetary cores.
 394 *Geophys. J. Int.*, 201, 1–17.
- 395 Chyba, C. F., & Hand, K. P. (2005). Astrobiology: The Study of the Living Universe.
 396 *Annu. Rev. Astron. Astrophys.*, 43(1), 31–74.
- 397 Ecke, R. E., & Niemela, J. J. (2014). Heat Transport in the Geostrophic Regime of Rotating
 398 Rayleigh-Bénard Convection. *Phys. Rev. Lett.*, 113, 114301.
- 399 Ecke, R. E., & Shishkina, O. (2023). Turbulent Rotating Rayleigh-Bénard Convection.
 400 *Annu. Rev. Fluid Mech.*, 55, 603–38.
- 401 Gastine, T., & Aurnou, J. M. (2023). Latitudinal regionalization of rotating spherical shell
 402 convection. *J. Fluid Mech.*, 954, R1.
- 403 Gastine, T., Wicht, J., & Aubert, J. (2016). Scaling regimes in spherical shell rotating
 404 convection. *J. Fluid Mech.*, 808, 690–732.
- 405 Gastine, T., Wicht, J., & Aurnou, J. M. (2015). Turbulent Rayleigh-Bénard convection in
 406 spherical shells. *J. Fluid Mech.*, 778, 721–764.
- 407 Hemingway, D. J., & Mittal, T. (2019). Enceladus’s ice shell structure as a window on
 408 internal heat production. *ICARUS*, 332, 111–131.
- 409 Julien, K., Aurnou, J. M., Calkins, M. A., Knobloch, E., Marti, P., Stellmach, S., & Vasil,
 410 G. M. (2016). A nonlinear model for rotationally constrained convection with Ekman
 411 pumping. *J. Fluid Mech.*, 798, 50–87.
- 412 Julien, K., Knobloch, E., Rubio, A. M., & Vasil, G. M. (2012). Heat transport in low-
 413 Rossby-number Rayleigh-Bénard convection. *Phys. Rev. Lett.*, 109(25), 254503.
- 414 Julien, K., Legg, S., McWilliams, J., & Werne, J. (1996). Rapidly rotating Rayleigh-Bénard
 415 convection. *J. Fluid Mech.*, 322, 243–273.
- 416 Julien, K., Rubio, A., Grooms, I., & Knobloch, E. (2012). Statistical and physical balances
 417 in low Rossby number Rayleigh-Bénard convection. *Geophys. Astrophys. Fluid Dyn.*,
 418 106, 392–428.
- 419 Kang, W. (2022). Different Ice-shell Geometries on Europa and Enceladus due to Their
 420 Different Sizes: Impacts of Ocean Heat Transport. *Astrophys. J.*, 934(2), 116.
- 421 Kang, W., & Jansen, M. (2022). On Icy Ocean Worlds, Size Controls Ice Shell Geometry.
 422 *Astrophys. J.*, 935(2), 103.
- 423 Kihoulou, M., Čadek, O., Kvorka, J., Kalousová, K., Choblet, G., & Tobie, G. (2023).
 424 Topographic response to ocean heat flux anomaly on the icy moons of Jupiter and
 425 Saturn. *ICARUS*, 391, 115337.
- 426 King, E. M., Stellmach, S., & Aurnou, J. M. (2012). Heat transfer by rapidly rotating
 427 Rayleigh-Bénard convection. *J. Fluid Mech.*, 691, 568–582.
- 428 King, E. M., Stellmach, S., & Buffett, B. (2013). Scaling behaviour in Rayleigh-Bénard
 429 convection with and without rotation. *J. Fluid Mech.*, 717, 449–471.
- 430 Kunnen, R. P. J. (2021). The geostrophic regime of rapidly rotating turbulent convection.
 431 *J. Turbul.*, 22, 267–296.

- 432 Kunnen, R. P. J., Clercx, H. J. H., & Geurts, B. J. (2006). Heat flux intensification by
433 vortical flow localization in rotating convection. *Phys. Rev. E*, *74*, 056306.
- 434 Kunnen, R. P. J., Stevens, R. J. A. M., Overkamp, J., Sun, C., Heijst, G. J. F. v., & Clercx,
435 H. J. H. (2011). The role of Stewartson and Ekman layers in turbulent rotating
436 Rayleigh-Bénard convection. *J. Fluid Mech.*, *688*, 422–442.
- 437 Nimmo, F., & Pappalardo, R. T. (2016). Ocean worlds in the outer solar system. *J.
438 Geophys. Res. Planets*, *121*(8), 1378–1399.
- 439 Plumley, M., & Julien, K. (2019). Scaling Laws in Rayleigh-Bénard Convection. *Earth
440 Space Sci.*, *6*(9), 1580–1592.
- 441 Plumley, M., Julien, K., Marti, P., & Stellmach, S. (2016). The effects of Ekman pumping
442 on quasi-geostrophic Rayleigh-Bénard convection. *J. Fluid Mech.*, *803*, 51–71.
- 443 Proudman, J. (1916). On the motion of solids in a liquid possessing vorticity. *Proc. R. Soc.
444 London A*, *92*, 408–424.
- 445 Roberts, P. H. (1968). On the thermal instability of a rotating-fluid sphere containing heat
446 sources. *Philos. Trans. R. Soc. A*, *263*(1136), 93–117.
- 447 Rossby, H. T. (1969). A study of Bénard convection with and without rotation. *J. Fluid
448 Mech.*, *36*, 309–335.
- 449 Santelli, L., Orlandi, P., & Verzicco, R. (2020). A finite-difference scheme for three-
450 dimensional incompressible flows in spherical coordinates. *J. Comput. Phys.*, *424*,
451 109848.
- 452 Shishkina, O., Stevens, R. J. A. M., Grossmann, S., & Lohse, D. (2010). Boundary
453 layer structure in turbulent thermal convection and its consequences for the required
454 numerical resolution. *New J. Phys.*, *12*, 075022.
- 455 Soderlund, K. M. (2019). Ocean Dynamics of Outer Solar System Satellites. *Geophys. Res.
456 Lett.*, *46*, 8700–8710.
- 457 Soderlund, K. M., King, E. M., & Aurnou, J. M. (2012). The influence of magnetic fields
458 in planetary dynamo models. *Earth Planet. Sci. Lett.*, *333-334*, 9–20.
- 459 Sprague, M., Julien, K., Knobloch, E., & Werne, J. (2006). Numerical simulation of an
460 asymptotically reduced system for rotationally constrained convection. *J. Fluid Mech.*,
461 *551*, 141–174.
- 462 Stellmach, S., Lischper, M., Julien, K., Vasil, G., Cheng, J. S., Ribeiro, A., ... Aurnou,
463 J. M. (2014). Approaching the Asymptotic Regime of Rapidly Rotating Convection:
464 Boundary Layers versus Interior Dynamics. *Phys. Rev. Lett.*, *113*, 254501.
- 465 Stevens, R. J. A. M., Blass, A., Zhu, X., Verzicco, R., & Lohse, D. (2018). Turbulent thermal
466 superstructures in Rayleigh-Bénard convection. *Phys. Rev. Fluids*, *3*, 041501(R).
- 467 Stevens, R. J. A. M., Clercx, H. J. H., & Lohse, D. (2010). Optimal Prandtl number for
468 heat transfer in rotating Rayleigh-Bénard convection. *New J. Phys.*, *12*, 075005.
- 469 Stevens, R. J. A. M., Clercx, H. J. H., & Lohse, D. (2013). Heat transport and flow structure
470 in rotating Rayleigh-Bénard convection. *Eur. J. Mech. B/Fluids*, *40*, 41–49.
- 471 Stevens, R. J. A. M., Zhong, J.-Q., Clercx, H. J. H., Ahlers, G., & Lohse, D. (2009).
472 Transitions between turbulent states in rotating Rayleigh-Bénard convection. *Phys.
473 Rev. Lett.*, *103*, 024503.
- 474 Taylor, G. I. (1917). Motion of solids in fluids when the flow is not irrotational. *Proc. R.
475 Soc. London A*, *93*(648), 99–113.
- 476 Taylor, G. I. (1923). Stability of a viscous liquid contained between two rotating cylinders.
477 *Phil. Trans. R. Soc. A*, *223*, 289–343.
- 478 Vance, S. D., Panning, M. P., Stähler, S., Cammarano, F., Bills, B. G., Tobie, G., ...
479 Banerdt, B. (2018). Geophysical Investigations of Habitability in Ice-Covered Ocean
480 Worlds. *J. Geophys. Res. Planets*, *123*(1), 180–205.
- 481 van der Poel, E. P., Stevens, R. J. A. M., & Lohse, D. (2013). Comparison between two
482 and three dimensional Rayleigh-Bénard convection. *J. Fluid Mech.*, *736*, 177–194.
- 483 Wang, G., Santelli, L., Lohse, D., Verzicco, R., & Stevens, R. J. A. M. (2021). Diffusion-free
484 scaling in rotating spherical Rayleigh-Bénard convection. *Geophys. Res. Lett.*, *48*(20),
485 e2021GL095017.

- 486 Wang, G., Santelli, L., Verzicco, R., Lohse, D., & Stevens, R. J. A. M. (2022). Off-centre
487 gravity induces large-scale flow patterns in spherical Rayleigh–Bénard convection. *J.
488 Fluid Mech.*, *942*, A21.
- 489 Weiss, S., Stevens, R. J. A. M., Zhong, J.-Q., Clercx, H. J. H., Lohse, D., & Ahlers,
490 G. (2010). Finite-size effects lead to supercritical bifurcations in turbulent rotating
491 Rayleigh–Bénard convection. *Phys. Rev. Lett.*, *105*, 224501.
- 492 Weiss, S., Wei, P., & Ahlers, G. (2016). Heat-transport enhancement in rotating turbulent
493 Rayleigh–Bénard convection. *Phys. Rev. E*, *93*, 043102.
- 494 Yang, Y., Verzicco, R., Lohse, D., & Stevens, R. J. A. M. (2020). What rotation
495 rate maximizes heat transport in rotating Rayleigh–Bénard convection with Prandtl
496 number larger than one? *Phys. Rev. Fluids*, *5*(5), 053501.
- 497 Zhong, J.-Q., Stevens, R. J. A. M., Clercx, H. J. H., Verzicco, R., Lohse, D., & Ahlers,
498 G. (2009). Prandtl-, Rayleigh-, and Rossby-number dependence of heat transport in
499 turbulent rotating Rayleigh–Bénard convection. *Phys. Rev. Lett.*, *102*, 044502.
- 500 Čadek, O., Souček, O., Běhounková, M., Choblet, G., Tobie, G., & Hron, J. (2019). Long-
501 term stability of Enceladus’ uneven ice shell. *ICARUS*, *319*, 476–484.